Nanoscale

ROYAL SOCIETY OF CHEMISTRY

PAPER

View Article Online
View Journal | View Issue

Cite this: *Nanoscale*, 2023, **15**, 13384

A study across scales to unveil microstructural regimes in the multivalent metal driven self-assembly of cellulose nanocrystals†

Valeria Gabrielli, Alberta Ferrarini * and Marco Frasconi *

Understanding the behaviour of self-assembled systems, from nanoscale building blocks to bulk materials, is a central theme for the rational design of high-performance materials. Herein, we revealed, at different length scales, how the self-assembly of TEMPO-oxidised cellulose nanocrystals (TOCNCs) into rod fractal gels is directed by the complexation of Fe^{3+} ions on the surface of colloidal particles. Different specificities in Fe^{3+} binding on the TOCNC surface and conformational changes of the nanocellulose chain were unveiled by paramagnetic NMR spectroscopy. The macroscopic properties of systems presenting different concentrations of TOCNCs and Fe^{3+} ions were investigated by rheology and microscopy, demonstrating the tunability of the self-assembly of cellulose nanorods driven by Fe^{3+} complexation. Near-atomistic coarse-grained molecular dynamics simulations were developed to gain microscopic insight into the behaviour of this colloidal system. We found that the formation of different self-assembled architectures is driven by metal–nanocellulose complexation combined with the attenuation of electrostatic repulsion and water structuration around cellulose, leading to different microstructural regimes, from isolated nanorods to disconnected rod fractal clusters and rod fractal gels. These findings lay the foundation to unlock the full potential of cellulose nanocrystals as sustainable building blocks to develop self-assembled materials with defined structural control for a range of advanced applications.

Received 27th March 2023,
Accepted 14th July 2023

DOI: 10.1039/d3nr01418e

rsc.li/nanoscale

Introduction

The hallmark of life is the assembly of individual and simple units into bigger and complex structures. Examples are DNA strands that pair, proteins that form quaternary structures, lipids that assemble into membranes and cells that form tissues.[1] Importantly, a pronounced difference can exist between the individual and collective behaviour of these units which, by acting in concert, are able to produce final complex architectures over various length scales.[2–5] Colloids are interesting systems with biomimetic behaviour in terms of self-aggregation.[3,6] Particularly, the self-assembly of polyelectrolytic colloids in the presence of ions in water solutions has been attributed to different mechanisms such as the formation of ion–colloid complexes, ion–ion correlations, and gradients of ionic strength or pH.[3,7] In addition to polyelectrolyte–ion interactions, a fine balance of polyelectrolyte–polyelectrolyte[8] and polyelectrolyte–water[8–11] intermolecular forces needs to be considered to fully understand the self-assembly of these systems. Therefore, to achieve insights into the structure–property correlation of these assembled systems, it is pivotal to conduct investigations that link atomistic, molecular, macromolecular and supramolecular level perspectives to the final material properties.[12]

To understand the complex self-assembly landscape of polyelectrolytic nanocolloids in the presence of salts, we opted to study the interaction between 2,2,6,6-tetramethylpiperidin-1-yloxyl (TEMPO)-oxidized cellulose nanocrystals (TOCNCs) and trivalent transition metal Fe^{3+} ions as a model system (Fig. 1). Cellulose nanocrystals (CNCs) are affordable, renewable, and biocompatible nanomaterials that are attractive for a wide range of applications given their outstanding mechanical and optical properties.[13–15] CNCs have a needle-like nanorod structure and, thanks to the presence of negative charges, form stable colloidal suspensions in water.[13,16] The negative charges on the CNC surface can either derive from the harsh hydrolysis of cellulose with sulfuric acid or from other chemical treatments, for example, with the TEMPO oxidant. Lastly, TOCNCs present a nearly regioselective modification of hydroxymethyl groups into carboxylic functional groups,[17] which was employed for functionalisation with different biomolecules[18] and polymers.[19] The negative charges on the CNC surface and on other TEMPO-oxidised nanocelluloses, such as TEMPO-oxi-

Department of Chemical Sciences, University of Padova, Via Marzolo 1, 35131 Padova, Italy. E-mail: alberta.ferrarini@unipd.it, marco.frasconi@unipd.it

† Electronic supplementary information (ESI) available. See DOI: https://doi.org/10.1039/d3nr01418e

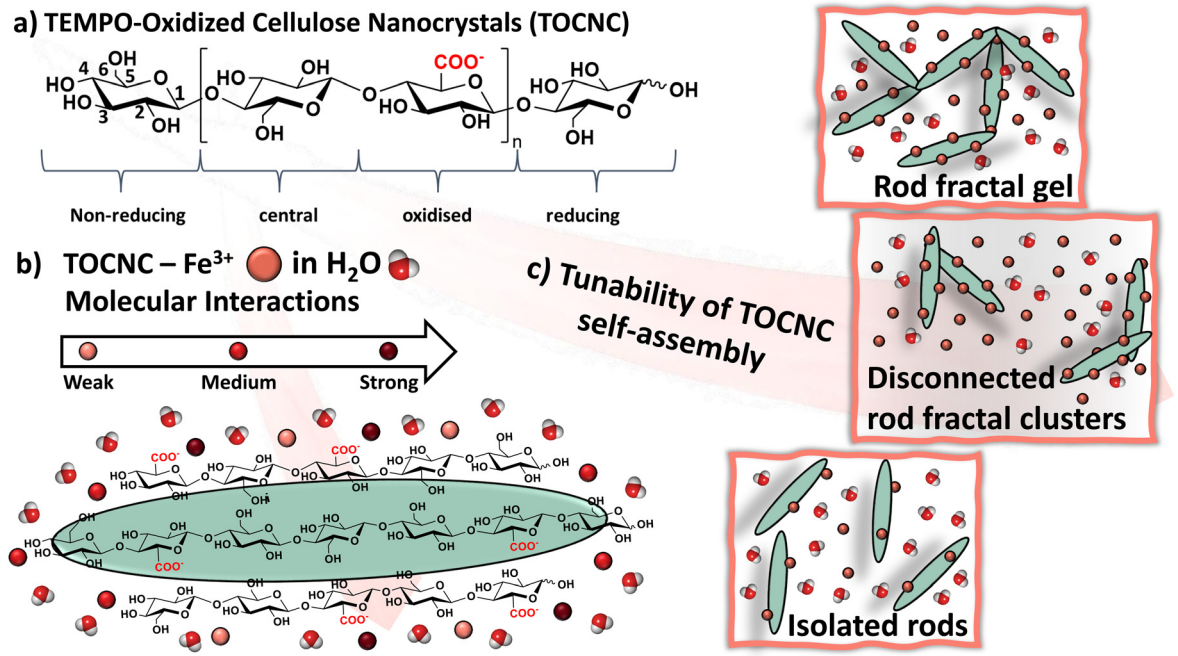

Fig. 1 (a) Chemical structure of TEMPO-oxidized cellulose with the corresponding spin systems highlighted by NMR spectroscopy. Numbering of the glucohexopyranose carbons is reported in the non-reducing ring. (b) Sketch of the interaction pathway between TOCNCs, Fe^{3+} ions and water molecules. (c) Coordination-driven self-assembly of TOCNCs and the formation of rod fractal gels from isolated rods with the transition through disconnected rod fractal clusters, controlled by the TOCNC and Fe^{3+} ion concentrations.

dised cellulose nanofibrils,[13] have shown binding affinity to alkali and transition metal ions leading to the formation of hydrogels.[20–22] The sol–gel transition of aqueous CNC suspensions in the presence of metal ions has been investigated by rheology and scattering techniques and the mechanism of formation of a 3D network has been proposed. At first, the negative repulsive forces generated by the carboxylate or sulphate surface charges of nanocellulose are screened by the metals present in solutions.[22] Sufficient screening then enables the particles to come close enough to establish van der Waals and other cohesive interactions, *i.e.*, coordination complexes with metal ions, and hydrogen bonding, that result in gelation.[23] This behaviour has been generally investigated in the presence of monovalent ions but deeper insight into the assembly mechanism in the presence of multivalent ions, able to establish specific interactions, is still missing.

Herein, the mechanism by which TOCNC nanorods form a 3D network in the presence of Fe^{3+} ions is proposed by using a combination of experimental investigations and computational modelling, offering a study across scales spanning from molecular interactions to macromolecular properties. In particular, the presence of Fe^{3+} ions allowed the use of paramagnetic NMR approaches unveiling the specific interaction between Fe^{3+} ions and the surface exposed carboxylic groups of TOCNCs and the cooperative contribution of the surrounding hydroxyl groups to the coordination of metal ions.

The redox behaviour of the coordination complex involving Fe^{3+} ions and TOCNCs has been investigated by cyclic voltammetry, showing the facile modulation of the complexation of the colloidal network by redox stimuli. Changes in macroscopic properties, finely tuned by different concentrations of cellulose and metal ions, have been fully characterized by rheology and scanning electron microscopy (SEM). Finally, the molecular mechanism behind the self-assembly of nanocellulose rods in the presence of Fe^{3+} ions, including the transition from isolated nanorods to disconnected rod fractal clusters and to rod fractal gels (Fig. 1), has been unveiled by molecular dynamics simulations with the MARTINI force-field. Even though initially developed for biomolecular simulations, nowadays, the MARTINI force-field finds extensive applications in the soft matter field.[24] MARTINI coarse-grained (CG) models of crystalline cellulose have been developed[25,26] and employed to investigate the molecular mechanism behind the change of allomorphicity.[25] The use of this chemically specific coarse-grained approach allowed us to reach an effective trade-off between all-atom models, which are necessarily limited to small cellulose fragments[8,21] or pairs of parallel short fibrils,[27] and supra coarse-grained models,[28,29] where chemical identities are lost. Overall, our investigation revealed unique insights into the self-assembly of TOCNC nanorods in the presence of Fe^{3+} ions. The approach proposed herein can easily be extended to the understanding of other colloidal associations in the presence of multivalent ions, opening the avenue to the next-generation bottom-up fabrication of functional, high-performance materials driven by structure–property relationships.

Experimental section

Materials

1 wt% TOCNC dispersion with a degree of oxidation of 1.9–2.0 mmol g^{-1} was purchased from Cellulose Lab (Canada). TOCNC nanorod dimensions were 8–15 nm in width and 100–150 nm in length. Iron(III) nitrate nonahydrate [$Fe(NO_3)_3{\cdot}9H_2O$; 98%] and deuterium oxide (D_2O, 99.9% atom D) were purchased from Sigma-Aldrich.

Sample preparation

The 1 wt% TOCNC dispersion was freeze-dried and the resulting solid was redispersed in Milli-Q water or D_2O. For NMR experiments, samples were prepared by adding defined aliquots of an Fe^{3+} stock solution (10 mM) to a 2 wt% dispersion of TOCNCs in D_2O under stirring. For rheology and SEM analysis, samples containing a 1 wt% or 3 wt% dispersion of TOCNCs were prepared in Milli-Q water, followed by the addition of an Fe^{3+} stock solution (100 mM) under stirring.

Nuclear magnetic resonance

All NMR experiments were performed using a Bruker DMX 600 MHz cryoprobe spectrometer operating at 600.13 MHz for ^1H NMR experiments and 150.90 MHz for ^{13}C NMR experiments, equipped with a 5 mm room-temperature TXI probe. Phase-sensitive 2D ^1H–^{13}C HSQC experiments were conducted *via* INEPT transfer using echo-antiecho and adiabatic pulses for inversion. An inter-pulse delay time of 3.44 ms ($\frac{1}{4}J_{CH}$) was used. Experiments set with a relaxation delay of 2 s were performed for 1 wt% TOCNC dispersion in the absence and presence of Fe^{3+} ions (1, 2, 3, 4 and 5 mM), collecting 128 $t1$ acquisitions with 48 scans per increment. In addition, HSQC experiments run with a relaxation delay of 60 s were performed for selected samples, collecting 64 $t1$ acquisitions with 16 scans per increment. The cross-peaks of the analysed samples were manually integrated to perform the analysis of the changes in the integral volume of the HSQC correlation peaks following a published procedure.[8] Phase-sensitive NOESY experiments with water suppression with gradients were carried out at 0, 100, 200, 300, 400, 500 and 600 ms mixing time with 128 increments in F1 with a relaxation delay of 2 s and acquisition of 16 scans. Each cross peak was divided by its corresponding diagonal peak at 0 ms. To monitor relative changes in the homonuclear dipolar coupling build-up of nearby protons, the absolute values were normalised against the highest cross-peak volume.

Saturation-transfer difference (STD) NMR experiments were performed at 298 K using a train of 50 ms Gaussian-shaped pulses. The on-resonance frequency for the selective saturation of the TOCNC network was set to −1 ppm,[10] while the off-resonance frequency for the acquisition of the reference spectrum was set to 50 ppm. For the TOCNC dispersion in the absence of Fe^{3+} ions, STD NMR experiments were performed using saturation times ranging from 0.25 to 8 s, with a constant time length per scan (saturation time and recycle delay) of 8 s. The number of scans (from 64 to 8) was inversely related to the saturation time. For TOCNC dispersions in the presence of Fe^{3+} ions, experiments with saturation times ranging from 0.05 to 5 s were performed with a constant time length per scan of 5 s. The acquired number of scans was inversely related to the saturation time (from 128 to 8 scans). Subtraction of the on-resonance (I_{sat}) spectra from the off-resonance (I_0) spectra resulted in the STD spectra (I_{STD}). The peak intensities of the I_{STD} difference spectrum were integrated relative to the peak intensities of the I_0 off-resonance spectrum to obtain the STD factor (ηSTD). For application of the Spin Diffusion Transfer Difference (SDTD) methodology, the obtained STD factors were normalised against the highest value and plotted against the square root of the saturation time ($t_{sat}^{1/2}$). The obtained SDTD build-up curves were then fitted to the SDTD equation (see eqn (4) in the ESI†), setting the r parameter to 2 Å and testing several values of the b parameter until the best fit was obtained.

Electrochemistry

Cyclic voltammetry experiments were performed with a potentiostat/galvanostat PGSTAT204 from Metrohm Autolab B.V. (The Netherlands), using a gold disk (diameter 2.0 mm), a platinum wire, and an Ag/AgCl/KCl 3 M as the working, auxiliary, and reference electrodes, respectively. Cyclic voltammetry was carried out at room temperature in a N_2-purged dispersion of TOCNCs (1 wt%) with Fe^{3+} at different concentrations in the presence of 100 mM Na_2SO_4 as an electrolyte.

Viscometry and oscillation rheology

The rheological properties were investigated using a Kinexus (Malvern Instruments) rheometer. Viscometry experiments were performed for 1 wt% TOCNC dispersion with a concentration of Fe^{3+} of 5 mM and 50 mM, and for 3 wt% TOCNC dispersion alone with 5 mM of Fe^{3+}, by using a cone-plate geometry and a shear rate range between 0.01 and 100 s^{-1}. Oscillatory rheology was performed with a parallel plate geometry on gels of 3 wt% TOCNC dispersion with 50 mM of Fe^{3+}. The linear viscoelastic region was determined by amplitude strain sweeps. Following this, dynamic frequency sweeps were performed with oscillatory frequencies between 0.1 and 100 Hz at a constant strain of 0.1%.

Scanning electron microscopy

Scanning electron microscopy (SEM) images were taken on a Zeiss Sigma HD microscope (5 kV), equipped with a Schottky FEG source, one detector for backscattered electrons, and two detectors for secondary electrons (InLens and Everhart Thornley). SEM samples were prepared by supercritical point drying and analysed without coating.

MD simulations

Coarse-grained molecular dynamics simulations using the MARTINI force-field have been developed, starting from an all-atom model, to investigate the self-assembly of TOCNC nanorods in the presence of different concentrations of Fe^{3+} ions in water (see Scheme S1† for an outline of the simulations).

Simulations were performed using the GROMACS2020.1 simulation package with the CG MARTINI_v2.3P force field, to which we added the PX atom type and the related self- and cross-term interactions.[25]

Results and discussion

Molecular interaction of Fe^{3+} ions with TOCNCs

At first, we recorded the 1D ^{1}H and 2D ^{1}H–^{13}C HSQC NMR spectra of 1 wt% TOCNC dispersions in the absence and presence of Fe^{3+} ions and monitored the disappearance of signals mediated by the paramagnetic relaxation enhancement (PRE) effect of Fe^{3+} ions. Acquisition of the ^{1}H NMR spectrum of TOCNCs revealed four different spin systems, namely the reducing (r), the non-reducing (nr), the central (c) and the oxidised (ox) spin systems (Fig. 1a), which could be unambiguously assigned (Fig. 2a, top projection in the ^{1}H–^{13}C HSQC spectrum). As shown in Fig. 2a, the ^{1}H–^{13}C HSQC spectra recorded in the presence of 5 mM Fe^{3+} ions show the disappearance of the peaks assigned to C3,5 of the oxidised ring, the C3, C4, and C5 of the non-reducing ring, the C2, C3, C4, and C5 of the reducing ring, and the C6 of the unfunctionalized central TOCNC residues. In addition, a reduction in cross-peak volume was recorded for all the other assigned carbons (C1c, C1r, C2c, C4c and C3,5c). As the PRE effect is distance-dependent, these data indicate a spatial proximity between the distinct TOCNC spin systems and the Fe^{3+} ions in the bound state. To monitor the reduction in the cross-peaks' volume, titration experiments with Fe^{3+} concentrations from 0 to 5 mM were performed. The decay of the signal of each isolated peak in the ^{1}H–^{13}C HSQC spectra was measured as the ratio of the cross-peak volume between the samples in the presence and absence of Fe^{3+} ions. All the reported ratios show values lower than one (Table S1†) and a linear decay (Fig. S1†), which could be ascribed to an increase in the fraction of TOCNC-bound Fe^{3+} ions upon increasing the Fe^{3+} concentration in the sample. Analysis of the slope of the lines shows a faster decay for C3,5ox, indicating a stronger binding of Fe^{3+} ions to the carboxyl residues. The second fastest decay was observed for the cross-peaks of the non-reducing and reducing residues, followed by the decay of the signals assigned to the C6 in unfunctionalized glucohexopyranose rings.

The different behaviour observed for the nanorod extremities could be attributed to either a more intimate interaction with the Fe^{3+} ions or their higher exposure to the surrounding solvent and ions.

To investigate the effect of Fe^{3+} ions on the conformation of residues on the TOCNC surface, 2D ^{1}H–^{1}H NOESY spectra in the absence and presence of Fe^{3+} ions (1 and 2 mM) were acquired at increasing mixing times (Fig. S2, S3 and S4†).[30] Significant changes in the normalised NOE build-up curve rates in the presence of Fe^{3+} ions were recorded for H1 to H6, H6′ and H3,5r (Fig. 2b), which might indicate a conformational rearrangement of the hydroxymethyl group and the inter-glycosidic linkage at that reducing ring following TOCNC–Fe^{3+}

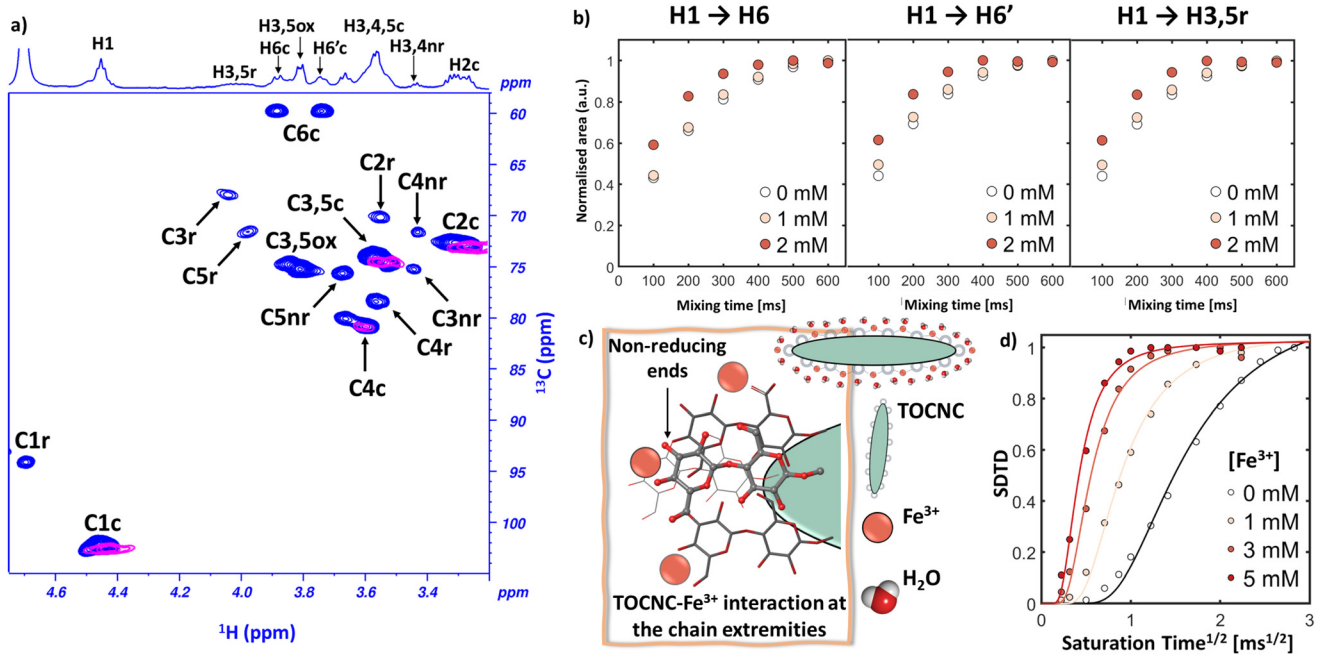

Fig. 2 (a) 2D ^{1}H–^{13}C HSQC NMR of 1 wt% TOCNC dispersion in D_2O in the absence (blue) and in the presence (pink) of 5 mM Fe^{3+} ions. The labels correspond to the reducing (r), non-reducing (nr), central (c) and oxidised (ox) rings, as shown in Fig. 1. (b) 2D ^{1}H–^{1}H NOESY build-up curves acquired at 25 °C for 1 wt% TOCNC dispersion at increasing Fe^{3+} ions concentrations. (c) Sketch of the intermolecular interactions established by the TOCNC nanorods with the Fe^{3+} ions in solution determined from NMR spectroscopy investigations. (d) SDTD curves of the HDO peak from 1 wt% TOCNC dispersion in the absence (black) and in the presence of Fe^{3+} ions at increasing concentrations (from yellow to dark red).

interaction. Protons H3,5ox, H3,4nr and H3,4,5c, in contrast, showed less pronounced changes (Fig. S4a and S4b†) or no changes at all (Fig. S4c†), inferring that, even upon binding of the Fe^{3+} ions to the carboxylic function, no significant conformational changes occurred. These NMR based investigations allowed us to obtain a detailed map of the interaction between TOCNCs and Fe^{3+} ions, as represented in Fig. 2c. In particular, Fe^{3+} ions interact with the carboxylic groups on the TOCNC surface, as well as with the diols of the glucohexopyranose units at the cellulose chain extremities and the hydroxymethyl group in the unfunctionalized glucohexopyranose residues. This is not surprising given their higher exposure to the environment and their ability to bind Fe^{3+}, as previously demonstrated for different carbohydrates[31] and also for catechol–Fe^{3+} complexes.[32]

The role of water on TOCNC–Fe^{3+} interaction

To probe the properties of water at the TOCNC interface upon introduction of the metal crosslinker we performed STD[33,34] and SDTD NMR experiments.[8,10,35] First, we collected STD build-up curves from TOCNC to HDO at increasing saturation times (Fig. S5†), and then we applied the SDTD NMR protocol.[10] From the SDTD NMR characterisation, we observed a stiffer slope of the SDTD curves upon addition of Fe^{3+} ions (Fig. 2d and Table S2†), which can be ascribed to a faster magnetization transfer from the gelator to the bound HDO and, therefore, to enhanced water structuration. The sudden increase in water structuration, observed upon the first addition of 1 mM Fe^{3+} ions, appears to gradually level out for higher Fe^{3+} concentrations, from 3 to 5 mM, which indicates the saturation of the effect between TOCNCs and HDO. From these results, it is clear that the interaction between TOCNCs and Fe^{3+} ions induces a tighter binding of HDO to the TOCNC surface or an increase in water confined among the TOCNC nanorods.

The redox behaviour of the TOCNC–Fe^{3+} complex

To understand the change of the redox properties of Fe^{3+} ions in complex with TOCNCs, we performed cyclic voltammetry (CV) measurements. Solutions of Fe^{3+} ions at different concentrations show a quasi-reversible behaviour, with the anodic and cathodic peaks at 0.61 V and 0.29 V *vs.* Ag/AgCl, respectively (Fig. S6†). When the CV of Fe^{3+} ions is performed in the presence of 1 wt% TOCNC dispersion, the Fe^{3+}/Fe^{2+} redox couple shows a more reversible electrochemical behaviour (Fig. 3a), with a shift of the anodic peak potential towards more negative values (0.49 V) compared to Fe^{3+} ions free in solution (0.61 V).

The peak-to-peak separation (ΔE_p, Fig. 3b) revealed that for low concentrations of Fe^{3+} ions, the presence of TOCNCs facilitates the electron transfer at the electrode–solution interface. In contrast, at a concentration of 10 mM of Fe^{3+} and above, in 1 wt% TOCNC dispersion, a larger peak separation is measured in comparison with Fe^{3+} free in solution (Fig. 3b). The larger variation in potential required with higher concentrations of Fe^{3+} ions could be attributed to the unbound of

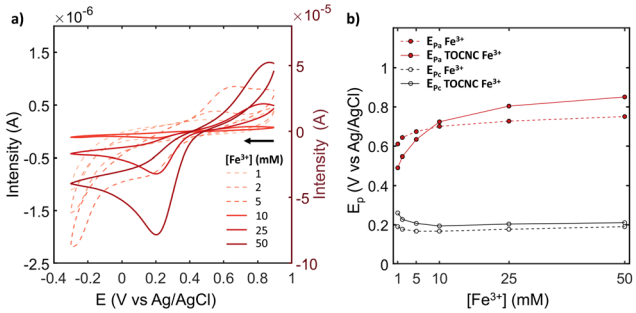

Fig. 3 (a) Cyclic voltammograms of 1 wt% TOCNC dispersions in the presence of various Fe^{3+} concentrations in a solution of 0.1 M Na_2SO_4 (scan rate of 0.01 V s^{-1}). The arrow indicates the scanning direction. Dashed-lines and solid-lines refer to the left and right *y*-axis, respectively. (b) Comparison of the anodic and cathodic peak potentials in the absence (gray) and in the presence (red) of TOCNCs with increasing concentrations of Fe^{3+} ions.

Fe^{3+} ions and the initial formation of aggregates of TOCNCs and Fe^{3+} ions at high concentrations. In contrast, the more positive oxidation potential of the 10 mM solution of free Fe^{3+} ions in comparison to the TOCNC–Fe^{3+} system, indicates a slower diffusion of the Fe^{3+} ions in the viscous TOCNC–Fe^{3+} solution. These results indicate that the oxidation/reduction reactions of the Fe^{3+}/Fe^{2+} redox couple occur at lower potentials and are more reversible in the presence of TOCNCs for low concentrations of Fe^{3+} ions, which can be attributed to the complexation-induced stabilization of the metal ions by TOCNCs.

The transition from a sol to gel of TOCNCs in the presence of Fe^{3+}

To probe the TOCNCs' ability to form hydrogels in the presence of Fe^{3+} ions, we performed experiments on 1 wt% (TOCNC1) and 3 wt% (TOCNC3) TOCNC suspensions at different Fe^{3+} concentrations, 0 (Fe0), 5 (Fe5) and 50 (Fe50) mM. The six resulting systems are henceforth labelled as TOCNC1Fe0, TOCNC1Fe5, TOCNC1Fe50, TOCNC3Fe0, TOCNC3Fe5 and TOCNC3Fe50. The formation of hydrogels occurred only for TOCNC3Fe50, while at lower TOCNC or lower Fe^{3+} concentrations we always observed a sol form. Changes in solution properties have been characterized by viscometry experiments. 1 wt% and 3 wt% TOCNC suspensions alone or in the presence of a low concentration of Fe^{3+} ions show a typical shear thinning behaviour at low shear rates, attributed to the alignment of the nanocrystals along the shear direction (Fig. 4a), and a Newtonian plateau at high shear rates, dictated by the complete alignment of the particles.[36] This result agrees with the electrochemical behaviour observed at low Fe^{3+} concentrations in TOCNC dispersions, where a higher reversibility of the CVs is obtained due to the formation of homogeneous TOCNC–Fe^{3+} complexes. Interestingly, a change in high viscosity shear thinning behaviour over the whole range of investigated shear rates has been observed for TOCNC1Fe50 (Fig. 4a). This transition suggests the presence of aggregates

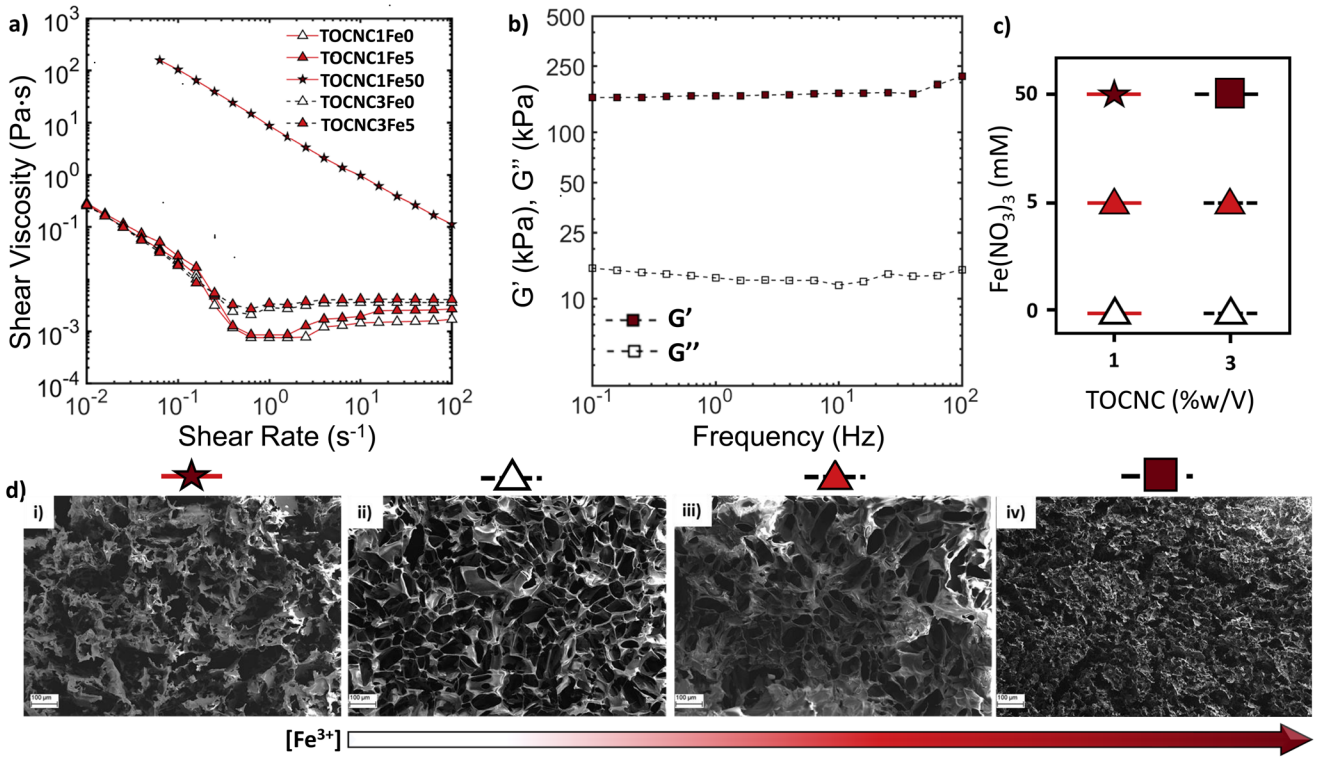

Fig. 4 Effect of TOCNC and Fe^{3+} concentrations on sol and gel formation. (a) Viscometry experiments of TOCNC1Fe0, TOCNC1Fe5, TOCNC1Fe50, TOCNC3Fe0 and TOCNC3Fe5. (b) Dynamic frequency sweeps for the TOCNC3Fe50 system. The variations in the storage moduli, G', and loss moduli, G'', are shown with closed and open symbols, respectively. (c) State diagrams for Fe^{3+} solutions of various concentrations added to the TOCNC dispersions of 1 wt% or 3 wt% concentrations. The low viscosity sol and gel states are indicated as triangles and squares, respectively. The star indicates the high viscosity sol. (d) SEM images (scale bar 100 μm) of (i) TOCNC1Fe50, (ii) TOCNC3Fe0, (iii) TOCNC3Fe5 and (iv) TOCNC3Fe50 systems. The images are labelled on top with the corresponding symbols in the state diagram.

within the system,[36] which is further supported by the electrochemical experiments performed on TOCNC dispersions at high Fe^{3+} concentrations. The properties of TOCNC3Fe50 gel, instead, were determined by oscillation rheology. In the investigated frequency range, G' values about one order of magnitude greater than G'' were measured, confirming the gel-like properties of the sample (Fig. 4b). In addition, both moduli showed little dependence on frequency in the studied range with a loss factor ($\tan\delta = G''/G'$) significantly smaller than unity, suggesting the formation of a stable gel with a dominant elastic behaviour and with minimal defects that would contribute to viscous energy loss.[21,22] A summary of the changes in the physical states of TOCNCs upon introduction of Fe^{3+} ions is reported in Fig. 4c.

To gain further insight into the sol–gel structures, SEM images of the TOCNC–Fe^{3+} sols and hydrogels have been acquired (Fig. 4d). The SEM images revealed a highly porous three-dimensional network created by the interconnection of the nanorods. In the case of TOCNC1Fe50, the large distribution of the area of the pores (Fig. S7†) is indicative of the preorganization of the nanorods into microstructures, even without reaching the degree of particle interpenetration required to create a gel structure. This finding aligns with the highly viscous rheological behaviour of the systems described above. The SEM images obtained for 3 wt% TOCNC dispersion in the absence and presence of Fe^{3+} (5 and 50 mM) show a decrease in the pore diameter from 43 μm for TOCNC3Fe5 to 29 μm for TOCNC3Fe50. The inverse correlation between the concentration of Fe^{3+} ions and the system porosity is in good agreement with the change from sol to gel observed by rheological investigation for the TOCNC3Fe50 system. This trend is consistent with the previously reported behaviour of CNC in the presence of monovalent ions, showing that suspensions with low concentrations of CNC (1 wt%) and salt (10 mM NaCl) form isolated clusters, while networks with densely aggregated rods result from higher concentrations of CNC and salt (5 wt% CNC and 100 mM NaCl).[37] In a recent study, Amini *et al.*[38] investigated the rheological behaviour of CNC hydrogels with different salts and found that the addition of divalent and trivalent ions enhances their viscoelastic properties, leading to a denser structure with smaller pores, which is in agreement with our results. In particular, for 5 wt% CNC in the presence of 100 mM Fe^{3+}, a uniform structure with pore sizes ranging between 31 and 47 μm was reported. The smaller pore size observed for our TOCNC3Fe50 system could be due to the stronger coordination of Fe^{3+} ions to the carboxylic groups present on the TOCNC surface.

Modelling the Fe^{3+}-driven self-assembly of TOCNCs

To gain further insight into the molecular mechanism behind the self-assembly of nanocellulose rods in the presence of Fe^{3+} ions, we carried out molecular dynamics (MD) simulations, using a coarse-grained approach based on the MARTINI 2 force-field.[39] Our cellulose nanocrystal model was built starting from the all-atom coordinates of cellulose Iβ fibrils.[40] In order to maintain the physical properties of the TOCNCs used in our experimental work (*i.e.*, crystal structure, aspect ratio, and charge density), we constructed TOCNC nanorods formed by 9 chains of cellulose (Fig. 5b, top), each composed of 20 repeating cellobiose units (Table S4†) and with a total number of 100 negative charges on their surface (Fig. 5b, bottom). Hence, cellulose chains were constructed by repetition of cellobiose units, each one described by 6 different beads (B1, B2, B3, B4, B5 and B6), and assigned to different types of beads (P1, P4 and PX) with distinct polar character (Fig. 5a and Table S3†), following the scheme proposed by López *et al.*[25] In addition, we introduced another kind of bead (BX, of bead type Qa), bearing a negative off-centred charge to represent the carboxyl groups (Fig. 5a and Table S4†). We performed MD simulations for three systems: (i) 2 rods of TOCNCs with 600 Fe^{3+} cations (TOCNC1Fe50), (ii) 6 rods of TOCNCs with 60 Fe^{3+} and 420 Na^{+} cations (TOCNC3Fe5) and (iii) 6 rods of TOCNCs with 600 Fe^{3+} cations (TOCNC3Fe50) (see ESI Tables S5 and S6†). The CG model, despite some inherent approximations, was able to capture differences in the ion–TOCNC interaction between the three systems. In all systems, cations were adsorbed on the surface of the rods, near the negative charges. Therefore, we calculated the average number of positive charges as a function of the distance from the centre of the BX beads (Fig. 5c(i), Fig. S8 and Table S7†). In both TOCNC1Fe50 and TOCNC3Fe50 this number is higher than 0.8, meaning that almost all charges on TOCNCs are screened and no electrostatic repulsion exists between the rods. In the system with a lower Fe^{3+} concentration (TOCNC3Fe5), in contrast, the average number of positive charges, coming from both Fe^{3+} and Na^{+} cations, amounts to about 0.6. Compared to Na^{+}, Fe^{3+} ions tend to stay slightly closer to the carboxyl groups (see Fig. S9†) and for longer times, as shown by the decay of the probability to remain in their proximity (Fig. 5c(ii)). Fig. 5c(ii) also shows some differences in the average survival probability of water near TOCNCs at high and low Fe^{3+} concentrations. This effect could be related to the increase in water structuring upon an increase in Fe^{3+} concentration as observed from the SDTD NMR experiments. MD simulations confirmed distinct self-assembly regimes for different combinations of TOCNC and Fe^{3+} concentrations, consistent with the experimental findings from rheology and SEM characterisation. In particular, TOCNC3Fe5 and TOCNC3Fe50 show different behaviours that reflect their rheological properties. In both cases, the same starting configuration was assumed, with the six rods randomly oriented (Fig. S10b and c†). In TOCNC3Fe5 during the trajectory the rods stay apart from each other and, even though they occasionally approach, then they move apart (Fig. 6a and Fig. S11a†). In TOCNC3Fe50, in contrast, in their random motion, rods can get closer and, when close enough, they form persistent contacts, which in most cases are bridged by Fe^{3+} ions (Fig. 5b and Fig. S11b†). Crossings in the system predominantly occur between the highly polar B1 and B5 beads, which correspond to the hydroxyl groups at positions C2 and C3 of the glucohexopyranose ring located at the ends of the nanorods. This observation aligns with the results of our ^{1}H–^{13}C HSQC and ^{1}H–^{1}H NOESY experiments. In TOCNC1Fe50 the two rods, initially nearly parallel at a distance of 100 Å from each other (Fig. S11b†), during the trajectory, approach and reach a distance of around 40 Å. However, the formation of persistent contacts was not observed, which can be ascribed to the low collision probability at a low density of rods. Overall, MD simulations offer a microscopic perspective on the findings from rheology and SEM experiments. At

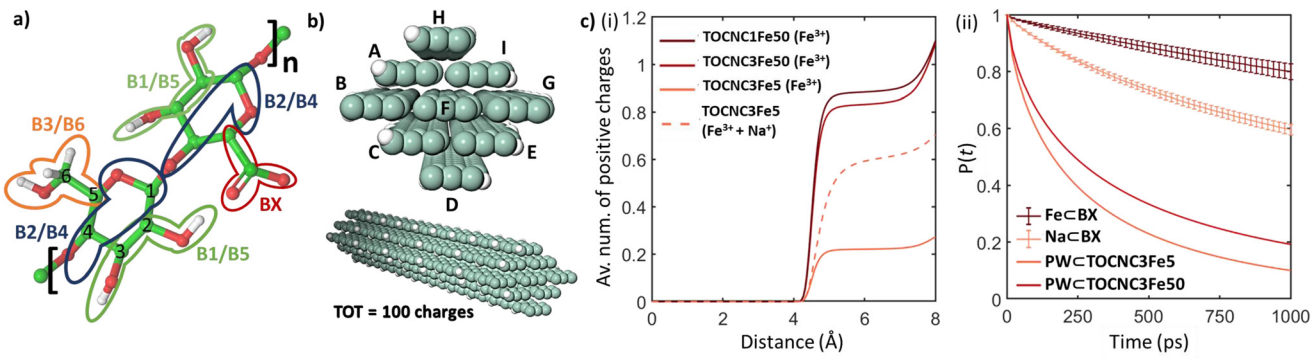

Fig. 5 (a) The cellobiose unit, representative of the cellulose chains, with the mapping of atoms to CG beads (B1, B2, B4, B5, BX, and P1). (b) Sketch of a TOCNC nanorod, formed by 9 cellulose chains (from A to I) of 40 glucohexopyranose units, each one comprising 3 CG beads. The white off-centered spheres are centered at the position of the negative charges on the TOCNC surface. (c) (i) Average number of positive charges as a function of the distance from the centre of BX beads for the TOCNC1Fe5, TOCNC3Fe5 and TOCNC3Fe50 systems. (ii) Survival probability, P(t), of Fe^{3+} and Na^{+} ions around (c) BX beads in the TOCNC3Fe5 model and of polarizable water (PW) around the cellulose nanorods for TOCNC3Fe5 and TOCNC3Fe50 systems. The error bars, not visible in the latter graphs, represent standard errors estimated by subdividing 50 ns trajectories into five equal parts.

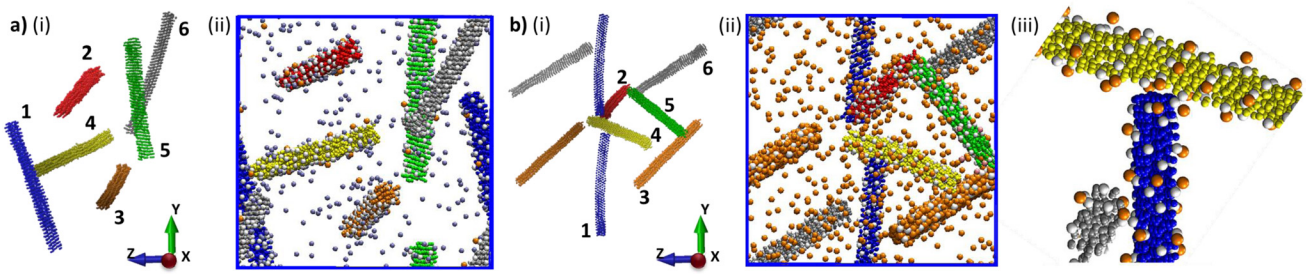

Fig. 6 Snapshots of (a) TOCNC3Fe5 and (b) TOCNC3Fe50 at the end of the MD trajectories showing (i) the configuration of the nanorods (the assigned rod numbers are reported); (ii) the whole system with the cations (Na^+ in ice blue and Fe^{3+} in orange); (iii) magnification of the contacts between ROD1, Fe^{3+} and ROD2, showing the ability of Fe^{3+} ions to bridge the cellulose nanorods. In the figures, the radius of the ions has been increased to facilitate visualization.

low Fe^{3+} concentrations, electrostatic repulsion between the rods hinders their approach, while at higher Fe^{3+} concentrations the negative surface charges of TOCNCs are effectively screened, allowing the rods to come into contact. Consequently, persistent connections are established through the Fe^{3+} ions leading to the formation of a physically crosslinked 3D network when the rod density is high enough (Fig. S12†). However, if the rod density falls within the dilute regime (volume fraction much smaller than the square of the aspect ratio),[41,42] only local contacts can be established, resulting in the formation of clusters comprised of crosslinked rods.

Conclusions

We established a model system to study the self-assembly behaviour of polyelectrolytic nanocellulose in the presence of multivalent transition metal ions across different length scales. We demonstrated that by varying the concentration of TOCNCs and Fe^{3+} ions, it is possible to tune the macroscale properties of the investigated systems from sol to gel. By NMR spectroscopy we showed that Fe^{3+} ions not only interact with the carboxylic function on the TOCNC surface, but also with the diols on the glucohexopyranose unit and, specifically, with the diols at the cellulose chain extremities. This result is in agreement with near-atomistic coarse-grained molecular dynamics simulations, which demonstrate the ability of TOCNCs to cross-link by means of the extremities through complexation with Fe^{3+} ions. In addition, we found a good correlation between the MD simulations and the changes in water structuration revealed by NMR spectroscopy. Furthermore, the combination of these simulations with rheological and microscopy (SEM) data allowed us to translate supramolecular associative interactions into the behaviour of a larger network, obtaining mechanistic insights into gel formation. Hence, we have understood how these rods progressively change microstructural regimes, from isolated nanorods to disconnected rod fractal clusters and rod fractal gels, with a consequent transition from sol to highly viscous sol to gel. Fe^{3+} ions play a twofold specific role: (i) they bind to the carboxylate groups, screening the negative charges on the TOCNC surface and suppressing the electrostatic repulsions that stabilise the colloidal suspension, and (ii) they drive the formation of a crosslinked network bridging pairs of rods. In addition, we demonstrated the electrochemical modulation of the properties of this TOCNC–Fe^{3+} system, which could pave the way for the development of new stimuli-responsive materials based on these metal-coordinated colloidal networks. To the best of our knowledge, this is the first time that such a detailed description of the mechanism of rod fractal gel formation, driven by the interaction between polyelectrolytic nanocellulose and multivalent transition metal ions, has been achieved. We have demonstrated that the application of the multiscale approach herein proposed enables one to achieve unique insights and to correlate molecular interactions, supramolecular architectures and material properties, expanding the toolbox for a study across scales of colloidal and, more generally, self-assembling systems.

Conflicts of interest

There are no conflicts to declare.

Acknowledgements

This research was supported by the University of Padova under the 2019 STARS Grant program “SensCo”. The authors thank Dr Andrea Basagni (University of Padova) for technical support in taking SEM images. Computational work has been carried out on the C3P HPC facility of the Department of Chemical Sciences of the University of Padova.

References

1 J.-M. Lehn, *Angew. Chem., Int. Ed.*, 2015, **54**, 3276–3289.
2 P. Romanczuk, M. Bär, W. Ebeling, B. Lindner and L. Schimansky-Geier, *Eur. Phys. J.: Spec. Top.*, 2012, **202**, 1–162.
3 W. Wang, W. Duan, S. Ahmed, A. Sen and T. E. Mallouk, *Acc. Chem. Res.*, 2015, **48**, 1938–1946.

4 M. M. J. Smulders, A. P. H. J. Schenning and E. W. Meijer, *J. Am. Chem. Soc.*, 2008, **130**, 606–611.
5 Y. Wang, P. J. Santos, J. M. Kubiak, X. Guo, M. S. Lee and R. J. Macfarlane, *J. Am. Chem. Soc.*, 2019, **141**, 13234–13243.
6 S. A. Mallory and A. Cacciuto, *J. Am. Chem. Soc.*, 2019, **141**, 2500–2507.
7 T. Benselfelt, M. Nordenström, M. M. Hamedi and L. Wågberg, *Nanoscale*, 2019, **11**, 3514–3520.
8 V. Gabrielli, R. Baretta, R. Pilot, A. Ferrarini and M. Frasconi, *Macromolecules*, 2022, **55**, 450–461.
9 J. Israelachvili and H. Wennerström, *Nature*, 1996, **379**, 219–225.
10 V. Gabrielli, A. Kuraite, M. A. Da Silva, K. J. Edler, J. Angulo, R. Nepravishta, J. C. Muñoz-García and Y. Z. Khimyak, *J. Colloid Interface Sci.*, 2021, **594**, 217–227.
11 B. L. Dargaville and D. W. Hutmacher, *Nat. Commun.*, 2022, **13**, 4222.
12 C.-C. Chou, F. J. Martin-Martinez, Z. Qin, P. B. Dennis, M. K. Gupta, R. R. Naik and M. J. Buehler, *ACS Nano*, 2017, **11**, 1858–1868.
13 D. Klemm, F. Kramer, S. Moritz, T. Lindström, M. Ankerfors, D. Gray and A. Dorris, *Angew. Chem., Int. Ed.*, 2011, **50**, 5438–5466.
14 G. Guidetti, S. Atifi, S. Vignolini and W. Y. Hamad, *Adv. Mater.*, 2016, **28**, 10042–10047.
15 D. Trache, M. H. Hussin, M. K. M. Haafiz and V. K. Thakur, *Nanoscale*, 2017, **9**, 1763–1786.
16 R. Ajdary, B. L. Tardy, B. D. Mattos, L. Bai and O. J. Rojas, *Adv. Mater.*, 2021, **33**, 2001085.
17 Y. Habibi, L. A. Lucia and O. J. Rojas, *Chem. Rev.*, 2010, **110**, 3479–3500.
18 V. Gabrielli, E. Missale, M. Cattelan, M. F. Pantano and M. Frasconi, *Mater. Today Chem.*, 2022, **24**, 100886.
19 H. Y. James, H. Lettow, P. F. Nealey and S. J. Rowan, *Macromolecules*, 2021, **54**, 10594–10604.
20 J. Schmitt, V. Calabrese, M. A. Da Silva, S. Lindhoud, V. Alfredsson, J. L. Scott and K. J. Edler, *Phys. Chem. Chem. Phys.*, 2018, **20**, 16012–16020.
21 H. Dong, J. F. Snyder, K. S. Williams and J. W. Andzelm, *Biomacromolecules*, 2013, **14**, 3338–3345.
22 M. Chau, S. E. Sriskandha, D. Pichugin, H. Thérien-Aubin, D. Nykypanchuk, G. Chauve, M. Méthot, J. Bouchard, O. Gang and E. Kumacheva, *Biomacromolecules*, 2015, **16**, 2455–2462.
23 F. Cherhal, F. Cousin and I. Capron, *Langmuir*, 2015, **31**, 5596–5602.
24 R. Alessandri, F. Grünewald and S. J. Marrink, *Adv. Mater.*, 2021, **33**, 2008635.
25 C. A. López, G. Bellesia, A. Redondo, P. Langan, S. P. S. Chundawat, B. E. Dale, S. J. Marrink and S. Gnanakaran, *J. Phys. Chem. B*, 2015, **119**, 465–473.
26 J. Wohlert and L. A. Berglund, *J. Chem. Theory Comput.*, 2011, **7**, 753–760.
27 A. Paajanen, Y. Sonavane, D. Ignasiak, J. A. Ketoja, T. Maloney and S. Paavilainen, *Cellulose*, 2016, **23**, 3449–3462.
28 A. Y. Mehandzhiyski, N. Rolland, M. Garg, J. Wohlert, M. Linares and I. Zozoulenko, *Cellulose*, 2020, **27**, 4221–4234.
29 N. Rolland, A. Y. Mehandzhiyski, M. Garg, M. Linares and I. V. Zozoulenko, *J. Chem. Theory Comput.*, 2020, **16**, 3699–3711.
30 V. Calabrese, J. C. Muñoz-García, J. Schmitt, M. A. Da Silva, J. L. Scott, J. Angulo, Y. Z. Khimyak and K. J. Edler, *J. Colloid Interface Sci.*, 2019, **535**, 205–213.
31 B. G. L. Nagy, *Coord. Chem. Rev.*, 2000, **203**(1), 81–149.
32 J. Yu, W. Wei, E. Danner, R. K. Ashley, J. N. Israelachvili and J. H. Waite, *Nat. Chem. Biol.*, 2011, **7**, 588–590.
33 M. Mayer and B. Meyer, *Angew. Chem., Int. Ed.*, 1999, **38**, 1784–1788.
34 M. Wallace, J. A. Iggo and D. J. Adams, *Soft Matter*, 2017, **13**, 1716–1727.
35 M. Martin-Pastor and E. Stoyanov, *J. Polym. Sci.*, 2023, **61**, 646–658.
36 S. Shafiei-Sabet, W. Y. Hamad and S. G. Hatzikiriakos, *Cellulose*, 2014, **21**, 3347–3359.
37 Y. Xu, A. D. Atrens and J. R. Stokes, *J. Colloid Interface Sci.*, 2017, **496**, 130–140.
38 M. Amini, M. Kamkar, F. Ahmadijokani, S. Ghaderi, O. J. Rojas, H. Hosseini and M. Arjmand, *Biomacromolecules*, 2023, **24**, 775–788.
39 S. J. Marrink, H. J. Risselada, S. Yefimov, D. P. Tieleman and A. H. De Vries, *J. Phys. Chem. B*, 2007, **111**, 7812–7824.
40 T. C. F. Gomes and M. S. Skaf, *J. Comput. Chem.*, 2012, **33**, 1338–1346.
41 H. Xu and S. Matysiak, *Chem. Commun.*, 2017, **53**, 7373–7376.
42 M. J. Solomon and P. T. Spicer, *Soft Matter*, 2010, **6**, 1391.